

1
2
3
4
5
6
7
8
9
10
11
12
13
14
15
16
17
18
19
20
21
22
23
24
25
26
27
28
29
30
31
32
33
34

Podiform magnetite ore(s) in the Sabzevar ophiolite (NE Iran): Oceanic hydrothermal alteration of a chromite deposit

Alireza Eslami^{1,2*}, Benjamin Malvoisin², Fabrice Brunet², Ali Kananian^{1*}, Wolfgang Bach³, Giovanni Grieco⁴, Alessandro Cavallo⁵, G. Diego Gatta⁴

¹School of Geology, College of Science, University of Tehran, Tehran 1417614418, Iran

²ISTerre, Univ. Grenoble Alpes, Univ. Savoie Mont Blanc, CNRS, IRD, IFSTTAR, 38041 Grenoble, France

E-mail addresses: alireza.eslami@univ-grenoble-alpes.fr

kananian@ut.ac.ir

³Geoscience Department, University of Bremen, Klagenfurter Str., 28359 Bremen, Germany

⁴Dipartimento di Scienze della Terra, Università degli Studi di Milano, via S. Botticelli 23, I-20133 Milano, Italy

⁵Dipartimento di Scienze dell'ambiente e del territorio e di Scienze della terra, Università di Milano-Bicocca, I-20126 Milano, Italy

Abstract

Serpentinite-hosted massive magnetite ore bodies are reported for the first time in the Late Cretaceous Sabzevar ophiolitic belt, northeastern of Iran. They show irregular and discontinuous shapes with variable sizes ranging from 30 to 60 cm. Chromian spinel grains are observed within both magnetite ores and host serpentinite. Magmatic chromian spinels, (Cr,Al)-spinel I, with compositions close to $(Mg_{0.6},Fe_{0.4})(Cr_{1.2},Al_{0.75},Fe^{3+}_{0.05})O_4$ are preserved in the host serpentinite where they display a porous alteration rim composed of Cr-bearing chlorite and three different spinel-structure minerals: Cr-spinel $(Fe_{0.6},Mg_{0.4})(Cr_{1.4},Al_{0.4},Fe^{3+}_{0.2})O_4$, named Cr-spinel II (second generation), magnetite and ferritchromite, nominally $FeCr_2O_4$. In the magnetite ore body, no (Cr,Al)-spinel I is found and Cr-spinel II occurs as relict cores surrounded by ferritchromite and magnetite. Detailed X-ray elemental mapping revealed that the 200 μm -thick magnetite rim is composed of two magnetite types with different minor element compositions: the first rim found at the contact with ferritchromite is thin (20 μm ; magnetite-I); the thicker outer rim contains numerous Fe-poor and Mg- and Si-rich silicate inclusions (magnetite-II). Observations at the TEM scale allows to identify ferritchromite which occurs as a micrometer-sized rim between Cr-spinel II and magnetite I. Thermodynamic modelling of the phase relationships in the

35 studied Sabzevar serpentinite suggests that Cr-spinel II is produced along with chlorite during a first
36 alteration stage at temperatures between 725 and 575 °C in the course of peridotite-water interactions.
37 A second hydrothermal alteration stage producing ferritchromite and magnetite is inferred from the
38 thermochemical modelling at temperatures < 400 °C under high H₂ fugacity. This latter stage
39 corresponds to the serpentinization of the Sabzevar oceanic peridotite and associated podiform
40 chromitite deposit. The two alteration stages are interpreted as the result of the interaction between
41 seawater and oceanic mantle at two different depth ranges in the course of its exhumation. Our
42 thermodynamic calculations and textural relationships revealed that Cr is immobile and Fe is the main
43 element to be transferred to the magnetite ore during alteration processes. Fe possibly originated from
44 direct transport of the Fe²⁺ produced during olivine dissolution or from the dissolution of nano-sized
45 magnetite grains initially formed in the host serpentinite during early serpentinization. Mass balance
46 calculation reveals significant iron transport at a scale > 10 m during serpentinization.

47

48 **Keywords:** Serpentinization; epitaxial growth; ferritchromite; iron segregation; ASTAR

49

50 1. Introduction

51 Magnetite ore bodies hosted by serpentinites have been described in several ophiolites
52 worldwide, in Morocco (Bou-Azzer, e.g. Gahlan et al., 2006; Gahlan and Arai, 2007), in Greece
53 (Olympus, Vermion, Edessa and Skyros Island; Paraskevopoulos and Economou, 1980), in central Iran
54 (Nain; Eslami et al., 2018a), in the Bangong–Nujiang suture zone in Tibetan Plateau (Angwu, Cebojiyi,
55 Beila, and Daru Co; Liu et al., 2019), in Southern Oman (Aniba; Khedr and Arai, 2018) and in the
56 Western Alps (Southern Aosta Valley; Rossetti et al., 2009; Carbonin et al., 2015; Della Guista et al.
57 2011; Toffolo et al., 2017) among others. In all these occurrences, magnetite ores form massive, nodular
58 and banded ores with an overall thickness that can vary from a few centimeters up to 50 m and with
59 lengths typically between 2 and > 500 m. The processes involved in such a large iron segregation, and
60 their driving forces remain poorly understood and the characterization at various scales of serpentinite-
61 hosted magnetite ores is therefore needed.

62 Magnetite ore formation can also be associated with magmatic spinel alteration. Spinel
63 composition is often used to determine the melting degree in residual peridotites (Dick and Bullen,
64 1984), along with mantle oxygen fugacity (O’Neil and Wall, 1987). The application of these two widely
65 used proxies requires deciphering the modification of the original spinel composition by late magmatic
66 processes, hydrothermal alteration and/or metamorphism.

67 It is well established that the hydrothermal alteration of peridotites at temperatures below 400
68 °C (i.e. serpentinization) induces the oxidation of the iron initially contained in olivine and pyroxene,

69 leading to magnetite formation (e.g., Moody, 1976; Oufi et al., 2002). Magnetite is often found as
70 disseminated grains in the serpentinite matrix or concentrated in mesh textures and in veins implying a
71 certain extent of remobilization (Beard et al., 2009). A first possible view is that the formation of large
72 ore bodies during serpentinitization (or during a later metamorphic stage), implies iron mobilization at a
73 large scale (e.g. Gahlan et al., 2006; Eslami et al., 2018a). Olivine and pyroxene serpentinitization could
74 then be the source of that iron (Prabhakar and Bhattacharya, 2013). The respective role of water/rock
75 ratio, temperature, oxygen fugacity and chemical potential gradients in driving this wide iron
76 segregation still needs to be clarified.

77 In serpentinite-hosted magnetite ores, magmatic chromium spinels, $(\text{Mg,Fe})(\text{Al,Cr,Fe})_2\text{O}_4$, may also
78 play a key role in magnetite formation (e.g. Kimball, 1990; Colas et al., 2019), as they are commonly
79 found in the core of the magnetite grains (Michailidis, 1990; Barnes, 2000; Barra et al., 2014). However,
80 the link between magnetite formation and Cr-spinel alteration is strongly debated.

81 Thermodynamic modelling predicts the formation of magnetite and ferritchromite (FeCr_2O_4) at the
82 expense of Cr-spinel at temperatures below $\sim 550^\circ\text{C}$ (Sack and Ghiorso, 1991). Hence, the iron involved
83 in magnetite formation at the Cr-spinel surface could be derived locally from Cr-spinel dissolution
84 (Ulmer, 1974). The formation of magnetite and ferritchromite at the expense of Cr-spinel requires
85 reactions in an open chemical system with Al and Cr removal or dilution. These two elements are often
86 considered as largely immobile in geochemical processes. The solubility, and thus the mobility, of Cr
87 depends on its oxidation state and on the presence of ligands, such as chlorine, which can complex
88 chromium and enhance its solubility (Huang et al., 2019). Divalent and hexavalent chromium are
89 actually orders of magnitude more soluble than trivalent chromium, Cr(III). The same type of solubility
90 contrasts holds also true for Fe (II) and Fe(III), and therefore redox potential (or oxygen fugacity) has
91 been logically identified as a key parameter in the formation of serpentinite-hosted magnetite ores.
92 Indeed, redox conditions may vary considerably depending on whether the magnetite ore formed during
93 serpentinitization, which would produce H_2 (Kimball, 1990), or during late stage fluid-rock interactions
94 under more oxidizing conditions (Gervilla et al., 2012; Barra et al., 2014).

95 Here, for the first time, we report a distinct suite of m-scale pod-like bodies of massive-textured
96 magnetite with a cataclastic fabric from the Late Cretaceous Sabzevar ophiolite in NE Iran. These
97 magnetite ore bodies share striking resemblances to podiform chromitite deposits reported throughout
98 the Sabzevar ophiolite belt by virtue of their common geological setting, analogous morphology and
99 macroscopic characteristics. Serpentinized dunite encompasses the podiform magnetite and chromitite
100 in the form of envelopes of variable thickness (≥ 0.5 m). Chromium-rich spinel is occasionally found as
101 relict core of magnetite grains inside the magnetite ore suggesting that the magnetite ores represent the
102 transformation products of pre-existing semi-massive or weakly disseminated chromitite. Spinel in both
103 magnetite ore and host serpentinite shows an intricacy of mineralogical, structural and geochemical
104 fingerprints resulting from a multi-stage alteration history.

105 We present here a detailed mineralogical description of the new magnetite ore occurrence with a
106 particular emphasis on the micro-nanotextural relationship between chromite and magnetite in both
107 magnetite ore and host serpentinite. Both phase relationships in the host serpentinite and fluid
108 compositions were modeled in order to interpret the micro- and nanoscale observation. A conceptual
109 model for the genesis of magnetite ore in the Sabzevar ophiolite is eventually proposed that involves
110 significant iron mass transfer from the serpentinite to the magnetite ore.

111

112 **2. Geological setting and magnetite-ore occurrence**

113

114 Several podiform chromitite ores have been described in the western and central part of the
115 Sabzevar ophiolite (Shafaii Moghadam et al., 2013, 2015). Here we describe a first occurrence of
116 podiform magnetite ores in the eastern sector (N36°32'55", E57°00'00") of the northern Sabzevar
117 ophiolite belt (called Sabzevar ophiolite). Sabzevar ophiolite shows a general SE-NW trend and it forms
118 a continuous belt, about 150 km long, consisting of thrust-bounded blocks of Neotethyan oceanic
119 lithosphere (Fig. 1b). The Sabzevar ophiolitic belt is often interpreted as having formed in an arc-related
120 oceanic basin (e.g., Noghreyan, 1982; Jafari et al., 2013; Shafaii Moghadam et al., 2015; Omrani, 2018;
121 Rahmani et al., 2020). More specifically, Sabzevar ophiolites are believed to represent an embryonic,
122 subduction-related oceanic basin that opened between the Lut Block to the South and Turan block to the
123 North since at least mid-Cretaceous time (Shafaii Moghadam et al., 2014).

124 The eastern sector of the Sabzevar ophiolite is dominantly composed of a km-scale peridotite
125 massif, which is locally crosscut by rodingitized microgabbroic-diabasic dykes, by gabbroic intrusions
126 and by Middle Eocene dacitic domes (Fig. 1c). Seafloor alteration and low-grade metamorphism have
127 been recorded in basaltic sequence of the Sabzevar ophiolite (Shojaat et al., 2003). Such modification
128 can be tracked in diabase and metasomatized (spilitic) pillow lavas in the studied area. Although
129 occurrences of retrogressed mafic granulitic bodies embedded in ophiolitic nappes have been reported
130 from the northern parts of the Sabzevar ophiolite (Rossetti et al., 2010), there is no indication of high
131 pressure metamorphism in the study area. We observed several massive and rarely disseminated pod-
132 like chromitite bodies ranging from a few centimeters to a few tens of meters in diameter. They are
133 hosted in dismembered masses of harzburgite in a brittle shear zone. Irregular and discontinuous trails
134 of podiform magnetite-ore bodies occurred within highly sheared serpentinite masses (Fig. 2a). These
135 ores occur as a series of boudins and elongated lenses that can be tracked over a distance of a few tens
136 of meters along a roadcut.. The contacts between the magnetite ores and the host serpentinite are usually
137 sharp (Fig. 2b). Small aggregated masses of octahedral magnetite crystals with variable sizes are barely
138 visible to the naked eye on hand specimen (Fig. 2c).

139 3. Methods

140 3.1 Bulk sample characterization

141 In total, nine specimens from individual magnetite pods and six samples from the host
142 serpentinites were collected in the studied area (Fig. 2). Polished thin-sections of the corresponding
143 samples were examined under transmitted and reflected light using a Leica optical microscope.

144 All collected rock samples were also crushed using a hydraulic press down to a grain size ≤ 2
145 mm. Subsequently, the granular material was milled with an agate ball mill for 15 minutes at 500
146 revolutions per minute. The obtained powders from each sample were mixed and quartered for the
147 preliminary measurement of LOI (loss on ignition).

148 Major element concentrations and loss-on-ignition (LOI) of the host peridotite bulk samples (MG21,
149 MG20 and MG16) were determined at the University of Milan Bicocca. Major element concentrations
150 were measured by energy-dispersive X-ray fluorescence (EDXRF) on fused glass disks with a
151 PANalytical Epsilon 3-XL spectrometer. The collected data were preliminary analyzed with the
152 Malvern Panalytical Epsilon 3 software platform, using the Omnian - standardless model, which
153 allows qualitative and quantitative chemical analysis of unknown materials without the construction
154 of calibration lines. The quantitative analysis was then repeated in 6 different instrumental conditions,
155 using the Panalytical WROXI[®] – synthetic, high quality Certified Reference Materials for calibration.

156

157

158 3.2 Micro- and nano-scale characterization

159 Quantitative chemical analyses of individual spinel and silicate minerals were collected using a
160 JEOL JXA-8230 electron probe micro-analyzer (EPMA) equipped with five wavelength-dispersive
161 spectrometers (WDS) and an energy-dispersive spectrometer (EDS) at the Institut des Sciences de la
162 Terre, University Grenoble Alpes, France. Analyses were performed at 15 kV acceleration voltage, 100
163 nA beam current and a beam size with a diameter of $\sim 1 \mu\text{m}$. The concentrations of minor and trace
164 elements (Si, V, Ti, Ni, Co, Mn and Zn) and major elements (Fe, Cr, Al and Mg) were measured by
165 WDS and EDS, respectively. Total counting times (peak plus background) were 440 s for Si $K\alpha$; 240 s
166 for V $K\alpha$, Ti $K\alpha$; 360 s for Co $K\alpha$; 180 s for Zn $K\alpha$; 100 s for Ni $K\alpha$ and Mn $K\alpha$. Natural minerals, pure
167 metals and synthetic oxides were used as standards and the ZAF correction was applied. Spectral
168 interference (V $K\alpha$ vs Ti $K\beta$) was corrected using the JEOL software-calculated correction factor. The
169 detection limits varied between 0.005 and 0.02 wt%, using 3-sigma criterion (Batanova and al., 2018).
170 Elemental distribution maps were collected using an accelerating voltage of 15 kV, a beam current of
171 200 nA and a dwell time of 700 ms.

172 Sulfide phases were analyzed using a four-WDS spectrometer CAMECA SX100 electron
173 microprobe analyzer (EMPA) at Department of Geosciences, University of Bremen, Germany.
174 Accelerating voltages of 20 kV and beam current of 20 nA were used. Peak counting times varied
175 between 20 and 40 s per element. The reference materials included synthetic compounds (i.e., Co, ZnS,
176 and FeS₂) as well as mineral standards (As: arsenopyrite, Mn: ilmenite, Fe: pyrite, Co: native cobalt, Ni:
177 native nickel, Cu: chalcopyrite, Zn: sphalerite, S: pyrite, Pb: galena, Sb: antimonite).

178 Chromite/magnetite contacts were characterized at the nanoscale in the magnetite ore by
179 Transmission Electron Microscopy (TEM). A TEM lamella was first extracted from a petrographic thin
180 section across a reaction zone surrounding chromite (sample MG15, location on Fig. 5) and thinned to
181 < 100 nm with a Ga⁺ focused ion beam using a ZeissTMNVision 40 Crossbeam at the Interdisciplinary
182 Center for Electron Microscopy (CIME⁻-EPFL, Lausanne, Switzerland). After attaching the TEM foil to
183 a copper grid, we acquired high-angle annular dark-field images (HAADF) and high-resolution images
184 (HRTEM) with a TecnaiTMOsiris microscope operated at 200 keV (CIME⁻ - EPFL, Lausanne). The
185 composition at the chromite/magnetite interfaces was determined by combining Scanning Transmission
186 Electron Imaging (STEM) with Energy Dispersive Spectrometry (EDS) mapping using a Field Electron
187 Gun JEOLTM 2100F TEM operated at 200 keV (CMTC, Grenoble, France). The maps were corrected
188 for thickness variation by scaling the number of counts with the oxygen map. This latter instrument was
189 also used in combination with an automatic crystallographic orientation tool (ASTARTM; Rauch and
190 Véron, 2014) to acquire crystal orientation maps at the nanoscale. A 1.5 nm-wide electron beam was
191 scanned over the region of interest while acquiring diffraction patterns with a spacing of 4 nm on a 500
192 x 500 grid. The collected diffraction patterns were compared to pre-calculated templates generated for
193 chromite and magnetite. The best-matching template was used for indexation at each pixel in order to
194 determine crystallographic orientation. The crystallographic data of Santos et al. (2005) were used for
195 generating the chromite templates. The magnetite templates were generated from a mineral structure
196 determined on a magnetite collected in the magnetite ore with X-ray diffraction data collected with an
197 OxfordTM Diffraction Xcalibur-1 diffractometer at the University of Milan.

198 Serpentine minerals were characterized using a Horiba Jobin Yvon LabRAM HR Evolution
199 micro-Raman spectrometer at the University of Milan Bicocca. Spectra were collected using a green Nd
200 532-nm laser source at a maximum output power of 300 mW. For each thin section, serpentine mineral
201 determination relied on the analysis of about hundred different serpentine areas.

202 **3.3 Thermodynamic modelling**

203 Temperature - f_{O_2} stability diagrams were calculated with Perple_X (version 6.9.0; Connolly,
204 2005) to investigate the influence of temperature and oxygen fugacity on Cr-spinel stability at 500 MPa.
205 The calculation was performed using the mean composition of the serpentinites collected in Sabzevar
206 (average on samples MG21, MG20 and MG16; Si 34.39 mol.%, Al 0.56 mol.%, Cr 0.26 mol.%, Fe 4.25

207 mol.%, Mg 60.45 mol.%, Ca 0.10 mol.%), and a water to rock ratio of ~ 1. The use of such compositions
208 to compute pseudosections implicitly requires to assume thermodynamic equilibrium at the centimeter
209 scale. Evans et al. (2013) have shown that the scale of equilibrium is probably smaller during
210 metasomatic events. The calculations performed here have thus to be seen as predictions of the state
211 towards which the rock should tend. The differences between the calculations and the observations will
212 serve for discussing element mobility during reaction. We used the thermodynamic database for solid
213 phases of Holland and Powell (2011) combined with the database of Sverjensky et al. (2014) for aqueous
214 species (DEW19HP622ver_elements.dat file). This database includes the dataset for chromium aqueous
215 species from Huang et al. (2019). It was extended by including the Fe-chromite and Mg-chromite
216 endmembers from Klemme et al. (2009). The fluid speciation was evaluated during the optimization
217 with lagged forward-calculations (Galvez et al., 2015). The mineral solid solutions considered were
218 olivine (O(HP); Holland and Powell, 1996, 1998), clinopyroxene (Cpx(HP); Holland and Powell, 1996,
219 1998), chlorite (Chl(HP); Holland and Powell, 1996, 1998), antigorite (Atg(PN); Padrón-Navarta et al.,
220 2013), brucite (B) and garnet (Grt(JH); Jennings and Holland, 2015). An additional solid solution was
221 built for Cr-bearing spinel by using a reciprocal model and the parameters for non-linearity in Gibbs
222 energy from Sack and Ghiorso (1991). This solid solution predicts a critical temperature of ~ 550°C for
223 the Fe₃O₄-FeCr₂O₄ solvus, which is consistent with the Sack and Ghiorso (1991)'s solid-solution model
224 (Fig. S1). The fluid was modelled with the generic molecular fluid equation of state of Perple_X
225 considering H₂O and H₂ as possible solvents. The thermodynamic database and solid solution model
226 files used in this study are provided in the Supplementary Materials.

227 The determination of the spinel composition evolution during cooling requires to estimate the fO_2 . All
228 oxygen fugacities are given relative to the fayalite-magnetite-quartz buffer (FMQ) as $\Delta\log_{10}fO_2$. Frost
229 (1985) proposed to calculate an internal fO_2 buffer for ultramafic rocks by fixing the activities in Fe in
230 the Fe-bearing phases (e.g. olivine, orthopyroxene and spinel). We used the same approach here but, as
231 the calculation is performed for a fixed bulk rock composition, determining the fO_2 only requires one
232 additional constraint on the composition. In the stability field of olivine (430 to 800°C), the fO_2 is
233 determined by using the Mg/(Mg+Fe) ratio of olivine as the additional compositional constraint. This
234 directly fixes the fO_2 in the divariant fields. In the trivariant fields, two fO_2 are calculated for a single
235 Mg/(Mg+Fe) ratio in olivine, one at $\Delta\log_{10}fO_2 > -3$ and the other at $\Delta\log_{10}fO_2 < -5$. We selected the
236 highest value of fO_2 which is continuous with the values determined in the divariant fields, and provides
237 values consistent with the estimates of Frost (1985). The Mg/(Mg+Fe) ratio measured in olivine relicts
238 found in the Sabzevar serpentinitized dunite is ~ 0.92. This value is systematically higher than the range
239 of ratios computed with the bulk rock composition of the Sabzevar serpentinite. To determine a bulk
240 rock composition consistent with the Mg/(Mg+Fe) ratio measured in olivine, we performed several
241 simulations with Fe contents higher than in the Sabzevar serpentinite. We selected the composition for
242 which 1) the value of 0.92 is encompassed in the calculated Mg/(Mg+Fe) ratio in olivine, and 2) the
243 spinel composition at 800°C is consistent with typical spinel composition from ophiolitic forearc

244 peridotite ($\text{Cr}^{3+} \sim \text{Al}^{3+}$; $\text{Fe}^{3+} < \text{Cr}^{3+}/\text{Al}^{3+}$). The iron concentration in the selected bulk rock composition
245 is by 20% higher than that of the analyzed Sabzevar serpentinite samples. This selected composition is
246 further used to determine the variation of fO_2 with temperature along the isopleth of Fo_{92} olivine
247 composition. At low temperature, where olivine is not stable, the additional compositional constraint
248 used to fix the fO_2 is the amount of oxygen in the system. It was considered to be equivalent to the
249 amount of oxygen in an assemblage composed of pure water and a ferrous peridotite (FeO only in the
250 bulk rock composition). Such an assemblage is expected to represent a mantle rock undergoing
251 serpentinization. The fO_2 determined with the two methods detailed above falls in the same range as the
252 fO_2 estimated by Frost (1985) in a cooling peridotite.

253 **4. Mineralogical and textural characteristics**

254 **4.1 Host serpentinite**

255 The host serpentinite displays a typical mesh texture, with olivine kernels of around 80 μm in
256 dimension, surrounded by serpentine and brucite. The scarcity of bastite suggests that the host protolith
257 was a dunite. Magnetite is rare and occurs as euhedral grains with sizes up to 150 μm . Raman
258 spectroscopy shows that serpentinite is composed of abundant polygonal serpentine (peak at 3697 cm^{-1}
259 and a shoulder at 3689 cm^{-1}) and lizardite (two intense peaks at 3683 and 3703 cm^{-1}), with minor
260 chrysotile (usually in veins, main peak at 3698 cm^{-1} with a shoulder at 3691 cm^{-1}).

261 Spinel from the Sabzevar host serpentinite shows two main alteration features. We will call
262 “*partly altered Al-spinel*”, the homogenous spinel single-crystals that are partly replaced along rim and
263 cracks by a secondary spinel matrix containing voids filled with magnetite + Al-bearing hydrous silicate
264 +/- brucite. This type of replacement texture is often called “porous” in the literature, due to the presence
265 of (filled) voids. A second type of spinel alteration texture in the Sabzevar host serpentinite corresponds
266 to entirely porous zones that lack any Al-spinel relict cores. This second type of texture will be called
267 *porous Cr-spinel*, hereafter, since the dominant spinel in this textural type is Cr-rich. Porous Cr-spinel
268 zones are strongly fractured and the average grain size is between 5 and 20 μm (Fig. 3b and 3.c). At the
269 microscale, the porous Cr-spinel matrix seems to be replaced by patches of Fe-chromite and magnetite
270 intergrowths (Fig. 3c), possibly indicative of a further alteration stage. Andradite occurs as skeletal
271 masses surrounding porous Cr-spinel in serpentinites (Fig. 3d). Fe-Ni alloys are finely dispersed around
272 spinel grains in the serpentine groundmass. Sulfide grains were not encountered in the studied
273 serpentinite samples.

274

275 **4.2 Magnetite ore**

276 The studied Sabzevar magnetite ores are heterogeneous in texture and consist of euhedral to
277 subhedral magnetite crystals with sizes from 5 to 500 μm (Fig. 2c). The silicate matrix is composed of
278 serpentine (70-80 vol.%), andradite (15-20 vol.%) and minor chlorite (< 5 vol.%). Relicts of spinel
279 surrounded by polycrystalline magnetite were found within all investigated magnetite ore samples. The
280 texture of these relict spinels can either be porous (Fig. 3e and f) as defined for serpentinite-hosted spinel
281 or massive (Fig. 3g). Magnetite around porous chromite can either be small newly-formed grains (Fig.
282 3f) or form a thick polycrystalline rim with serpentine +/- brucite inclusions (Fig. 3e). Euhedral
283 magnetite crystals can also be found as inclusion in andradite crystals (Fig. 3h). In a few cases, individual
284 andradite-rich veins cut through the magnetite ore. Sulfide minerals are sporadically dispersed in the
285 Sabzevar magnetite ores. Pentlandite, $(\text{Fe},\text{Ni})_9\text{S}_8$, with subordinate heazlewoodite, Ni_3S_2 , and
286 chalcopyrite are common sulfides. Pentlandite and heazlewoodite occur mainly as anhedral to subhedral
287 inclusions with variable sizes and/or as large aggregation in magnetite crystals (Fig. 3i).

288

289 4. Mineral chemistry

290 4.1 Spinel

291 The composition of spinel from magnetite ores and from the host serpentinites have been plotted
292 in a trivalent-cation (Fe^{3+} -Cr-Al) ternary plot as well as in binary $X_{\text{Cr}} - X_{\text{Mg}}$ and $\text{Fe}^{3+}/(\text{Fe}^{3+} + \text{Fe}^{2+}) - X_{\text{Mg}}$
293 diagrams (Fig. 4). The cores of partly altered Al-spinel have the lowest chromium number and the
294 highest Al content. They display compositions that are typical for spinel from ophiolitic forearc
295 peridotites (Fig. 4; Table S1).

296 In the serpentinite samples, spinels from the porous rim of partly altered Al-spinel and from
297 porous Cr-spinel matrix share strong chemical similarities and are most likely genetically related. They
298 both plot in the same regions of the compositional diagrams shown in Fig. 4. They are relatively depleted
299 in Al compared to the partly altered Al-spinel and enriched in chromium relatively. Patches of porous
300 chromite formed by transformation of the Cr-spinel porous matrix have also been plotted in Fig. 4. The
301 composition of porous and homogeneous chromite cores in the magnetite ores strongly resembles that
302 of Cr-spinel from the serpentinite samples (Fig. 4).

303 X-ray elemental maps, along with point microanalyses, were collected using the EPMA on
304 homogeneous and porous Cr-spinel relicts rimmed by magnetite (Figs. 5 and 6), from the magnetite ore
305 samples. The various elemental maps obtained on homogeneous chromite confirms its chemical
306 homogeneity at the minor elements level. On a chemical basis (Table S2; Figs. 5 and 6), two generations
307 of magnetite can be distinguished. A first magnetite rim is observed (called "magnetite-I rim") from the
308 Cr-spinel interface, which has a thickness of $\sim 20 \mu\text{m}$ and displays a SiO_2 content <1 wt.%, a Cr_2O_3

309 content of 2.70-3.69 wt.% and a TiO₂ content > 1 wt.%. A second magnetite rim (called “magnetite-II
310 rim”) has a variable thickness ranging from 40 to 200 μm, and shows a different composition reflecting
311 the presence of inclusions at the nanoscale. The SiO₂ content is higher and ranges from 1.21 to 2.35
312 wt.%. The MgO and Cr₂O₃ contents are variable in the 0.06-0.12 wt.% and 0.03-1.62 wt.% range,
313 respectively. The TiO₂ content is lower (< 0.47 wt.%). Titanium is heterogeneously distributed within
314 the magnetite-I rim, with the highest concentration close to the chromite – magnetite-I boundary. On the
315 elemental maps, the magnetite-I/II interface is sharp and seems to outline former crystal faces. Porous
316 chromite shows higher Al, Mn, Ni and V in comparison with homogenous chromite relicts (Table S2).
317 Mg- and Al-rich spotty zones in porous chromite outline the numerous chlorite inclusions (Fig. 6).

318 **4.2 Sulfides and alloys**

319 Chemical compositions of sulfides and alloys in the Sabzevar magnetite ores and
320 associated serpentinites are given in Table S3. Pentlandite displays a wide range of Co (7.53 - 27.12
321 wt.%), Ni (18.56 - 36.67 wt.%) and Fe (17.34 - 29.96 wt.%) contents. There is no obvious relationship
322 between composition and textural position of pentlandite. Average composition of heazlewoodite shows
323 Ni (74.03 wt.%), S (27.37 wt.%) and Co (0.17 wt.%). Fe–Ni alloys from the Sabzevar serpentinites show
324 a large range of compositions from Ni₇₃Fe₁₉ to Ni₈₀Fe₂₆, which can be classified as awaruite (Ni₃Fe).
325

326 **4.3 Andradite, chlorite and brucite**

327 Andradite in both magnetite ore and host serpentinite have similar chemical compositions (Table
328 S4). They are chemically homogeneous and characterized by TiO₂ content < 0.30 wt.%, Al₂O₃ contents
329 ranging between 0.40–1.15 wt.%, Cr₂O₃ contents between 0.04 - 1.20 wt.% and Fe₂O₃ contents
330 between 28.76 - 30.24 wt.% (Table 5). Chlorite inclusions in chromian spinels from the magnetite ores
331 have higher FeO contents (2.55 - 5.52 wt.%) compared to those in chromian spinel from the host
332 serpentinite (Table S5). Chlorite inclusions in chromian spinel from both magnetite ore and host
333 serpentinite display relatively high Cr₂O₃ content (2.30 - 5.02 wt.%) and variable Al₂O₃ content (6.66 -
334 14.74 wt.%) (Fig. 4a). Brucite in the Sabzevar host serpentinite has X_{Mg} values ranging from 0.60 to
335 0.75.

336 **5. Nanoscale characterization of the magnetite rims**

337 A lamella was cut across at the interface between Cr-spinel with homogeneous texture and
338 magnetite from the magnetite ore (sample MG15; black arrow in Fig. 5) for TEM characterization to
339 gain insight on the Cr-spinel alteration processes at the nanoscale. The contact between Cr-spinel with
340 homogeneous texture and magnetite can be divided into four zones (Fig. S2). At the lamella scale, Cr-
341 spinel is homogeneous in composition, Al-, Cr- and Mg-rich and relatively depleted in Fe (Table S2;

342 Fig. 7). This composition is consistent with EPMA analyses performed on the same grain (Fig. 4). It
343 contains a few subgrain boundaries. Automatic crystal orientation mapping reveals a homogeneous
344 orientation in Cr-spinel with a misorientation of less than 0.5° over a distance of $1\ \mu\text{m}$. STEM-EDS
345 mapping indicates that Cr-spinel is separated from magnetite-I by a $\sim 1\ \mu\text{m}$ thick rim of a phase which
346 could not be resolved with EPMA (Fig. 7a). This phase displays a Cr content similar to that of Cr-spinel
347 but contains lower Al and Mg and higher Fe contents (Fig. 7b to g). Such a composition recalls the
348 composition of ferritchromite from the host serpentinite. We therefore use in the following the same
349 nomenclature as for the host serpentinite. The contact between ferritchromite and magnetite-I is sharp
350 on STEM-EDS maps. Locally, the contact is marked with Ti-rich lenses with sizes below $50\ \text{nm}$ (Fig.
351 7f) which indicate that Ti is segregated through the precipitation of a Ti-rich phase (e.g., rutile). Bright
352 field and HAADF images do not allow to locate the Cr-spinel – magnetite-I boundary as clearly as with
353 STEM-EDS mapping (Fig. 7a).

354 The misorientation angles extracted from the orientation maps are of less than 3° and 0.5° at the
355 Cr-spinel – ferritchromite and the ferritchromite – magnetite-I interfaces, respectively (Fig. 8a). The
356 comparison of electron diffraction patterns (SAED) on both sides of the interface is in line with small
357 misorientation angles. Cr-spinel and ferritchromite display coherent planes (Fig. 8b). The high
358 resolution TEM images also show some continuous planes across the interface (Fig. 9a). The SAED
359 patterns of ferritchromite and magnetite-I are identical, indicating perfect epitaxy (Fig. 8c).

360 Magnetite-I is $\sim 10\ \mu\text{m}$ thick in the investigated region (Fig. S2). It is homogeneous in
361 composition and enriched in Si and Ti compared to Cr-spinel and ferritchromite. The nanostructure of
362 magnetite-I is complex with micrometer-wide grains surrounding regions composed of densely packed
363 $20\ \text{nm}$ -wide grains (Fig. S3). The contact between magnetite-I and magnetite-II is sharp. The two
364 magnetite types display similar composition (Fig. 10). Magnetite-II contains $100\ \text{nm}$ -wide and $300\ \text{nm}$ -
365 long, Fe-poor and Mg- and Si-rich inclusions, probably made by serpentine. These inclusions are likely
366 responsible for the high Si contents measured by EPMA (Figs. 4 and 5). The orientation of magnetite-I
367 and magnetite-II is different with a misorientation angle between the two phases of 35° (Fig. 8d). This
368 is confirmed on high-resolution images which show a steep angle between the lattice planes in
369 magnetite-I and magnetite-II (Fig. 9b).

370

371 **6. Thermodynamic modelling**

372 Phase relationships have been calculated on the Sabzevar serpentinite composition at $500\ \text{MPa}$ and
373 plotted in a $\Delta\log_{10}f\text{O}_2$ -T diagram (Fig. 11). Among the main features of this calculation, there is the
374 composition of the spinel solid solution(s), $(\text{Mg,Fe})(\text{Al,Fe,Cr})_2\text{O}_4$, which contains two redox sensitive
375 elements, Fe and Cr, and which is thus expected to be $f\text{O}_2$ dependent. Furthermore, a solvus in the
376 $\text{Fe}(\text{Fe,Cr})_2\text{O}_4$ spinel subsystem has been reported below ca. 550°C (Sack and Ghiorso, 1991), which is

377 thus relevant to the temperature range investigated here. The incorporation of chromium in garnet is also
378 accounted for by the garnet solid-solution considered here. Although chromium-bearing chlorite is also
379 likely to share phase relationships with Cr-spinel and Cr-bearing garnet, no Cr-chlorite component has
380 been considered in the chlorite solution used in the present calculation. Consequently, the stability field
381 of chlorite might be larger than predicted here.

382 We computed the composition of the spinel solid solution(s) along a cooling path divided in two
383 parts (Fig. 11). The oxygen fugacity in the high temperature part of the path (800 to 420°C) is internally
384 buffered by the olivine – Mg-silicate – spinel assemblage (Frost, 1985). The low-temperature part of the
385 path (420 to 300°C) considers a serpentinization reaction in which the amount of oxygen is fixed. The
386 bulk rock + fluid composition is assumed to be the one of a ferrous peridotite plus pure water. Such a
387 path provides a first-order estimate of the effect of temperature on spinel composition. At high
388 temperature and high fO_2 (800°C and $\Delta\log_{10}fO_2 = 0$, respectively), the single spinel solid-solution
389 contains mainly Mg as divalent cation (Fig. 12b) and ~ 60 % of Al as trivalent cation (Fig. 12a), leading
390 to simplified composition of $Mg(Fe_{0.1},Cr_{0.3},Al_{0.6})_2O_4$. At $T < 730$ °C, the Al content of the spinel strongly
391 decreases due to the formation of chlorite. As a result, the X_{Cr} of the spinel increases from 0.6 at ~730°C
392 to > 0.95 at ~ 600°C and below. At $T < 400$ °C, two spinels are predicted to form in association with
393 brucite, $(Mg,Fe)(OH)_2$. The first type of spinel has a composition close to that of the high temperature
394 spinel. Its $Cr/(Cr+Fe^{3+})$ ratio progressively increases from ~ 85% at 400°C to 95 % at 350 °C leading to
395 an $Mg(Fe_{0.05},Cr_{0.95})_2O_4$ composition. The second type of spinel is close to the magnetite end-member
396 since it contains mainly Fe^{3+} as trivalent cation and Fe^{2+} as divalent one. The formation of this near-
397 endmember magnetite occurs at the expense of olivine through serpentinization reactions (Fig. 11). The
398 amount of Mg among the divalent cations decreases from 70 down to 0 mol.% from 430 to 300 °C,
399 respectively. Simultaneously, the molar fraction of brucite in the solid increases from 6 to 84 mol.%
400 (0.1 to 5.9 wt.%; Fig. S4).

401 The composition of the aqueous solution has also been calculated for the same bulk-rock
402 composition and in the same $\Delta\log_{10}fO_2 - T$ range. The pH is slightly alkaline at low temperatures, as
403 expected for water interacting with an ultramafic lithology (Galvez et al., 2016). The pH decreases with
404 temperature from 2.5 pH units above neutral at 250°C to 0.5 pH units above neutral at 800°C. The
405 fraction of H_2 in the solvent increases as the temperature increases and as the oxygen fugacity decreases
406 . The concentration of dissolved iron is rather constant around 10^{-3} mol/kg along the cooling path
407 investigated here (Fig. 13 a). The dominant iron-bearing aqueous species are ferrous iron species.
408 $HFeO^{2-}_{,aq}$ dominates at T below 500 °C whereas $Fe(HSiO_3)^+$ dominates above 500 °C. Chromium
409 solubility is between 7 and 8 orders of magnitude lower than iron solubility (Fig. 13 b, Fig. S5 and S6).
410 Therefore, Cr must be considered as an insoluble element in the conditions investigated here. The Cr
411 aqueous species are dominated by trivalent chromium species, Cr(III), at relatively low oxygen fugacity
412 with $Cr(III)/(Cr(II) + Cr(III) + Cr(VI)) > 99\%$ in most of the investigated $\Delta\log_{10}fO_2 - T$ domain. Among

413 the Cr(III) species, $\text{Cr}(\text{OH})_{4,\text{aq}}^-$ dominates. Cr solubility is approximately one order of magnitude higher
414 at temperatures above 500 °C than at low temperature along the cooling path investigated here.

415

416 7. Discussion

417 7.1 Two-stage spinel alteration process

418 Three types of spinel were identified based on their microtexture and composition in the
419 serpentinite hosting the magnetite ores. We described the first type of microtexture as *partly altered*
420 *spinel*, which consists in a *homogeneous* Al-Cr spinel core (X_{Cr} of 0.6). The Al-Cr spinel core
421 composition falls at the end of the compositional range of magmatic spinels reported in the Sabzevar
422 ophiolite podiform chromitite deposits (Fig. 4), which derived from island arc tholeiites with boninitic
423 affinity (Shafaii Moghadam et al., 2015; Eslami et al. 2018b). Both textural relationships and
424 composition suggest that the Al-Cr spinel core in the partly altered type is a relict of magmatic spinel
425 that was possibly altered during magmatic processes. The magmatic part of the spinel history will
426 however not be discussed here. We will consider that these residual cores correspond to a first generation
427 of spinel and will thus be named (Cr,Al)-spinel-I in the following.

428 (Cr,Al)-spinel-I is partly replaced along rim and cracks by a *porous rim* composed of a
429 secondary Cr-spinel, or Cr-spinel-II, matrix (X_{Cr} of= 0.8) containing voids partially stuffed with Al-
430 bearing hydrous silicate +/- brucite. Besides the partly altered texture, other spinel-rich areas are found
431 which are, texturally, entirely porous (i.e., with no homogeneous core). Cr-spinel-II of the porous rim
432 of partly altered spinel and the spinel that composes the matrix of those fully porous areas have also
433 similar compositions. This suggests that these two spinel types are genetically related. The absence of a
434 homogeneous core in that case is interpreted as the result of the complete replacement of (Cr,Al)-spinel-
435 I leaving no relict behind in contrast to partly altered (Cr,Al)-spinel textures. Therefore, we did not
436 distinguish between the secondary Cr-spinels (Cr-spinel-II) in both textural types.

437 At the micrometer scale, the chromite found in the magnetite ore displays two types of
438 microtextures. They are either anhedral with a homogeneous composition (Fig. 5) or made by an
439 aggregate of subgrains leading to a porous microtexture (Fig. 6). The homogenous spinel grains are
440 surrounded by a magnetite rim, whereas such a rim is not systematically found around porous chromite
441 in the magnetite ores. The regions where rims are not found are strongly deformed. This may indicate
442 cataclasis, leading to a loss of the microtextural information necessary to link chromite and magnetite
443 formations. All chromite grains have identical composition similar to Cr-spinel-II from the host
444 serpentinite (Fig. 4). Moreover, some of them display a similar porous texture. Therefore, their
445 formation probably originates from the reaction of the same type of magmatic spinels as in the
446 serpentinite host. In that respect, we tentatively categorized them as Cr-spinel-II as well, even though,
447 we did not find patches of magnetite and/or ferritchromite in the porous chromite found in the magnetite
448 ores. Indeed, magnetite only occurs as a rim around the Cr-spinel-II core either homogeneous or porous.
449 A $\sim 1 \mu\text{m}$ thick spinel phase separates Cr-spinel-II from a first magnetite rim (magnetite-I). Its
450 composition is consistent with the ferritchromite analyses collected in the serpentinite (Al, Mg and Fe

451 contents intermediary between magnetite and Cr-spinel-II; Fig. 6). Ferritchromite and magnetite display
452 a perfect epitaxial relationship, suggesting mutual growth during the same alteration stage at the expense
453 of Cr-spinel-II. This type of pseudomorphic replacement of Cr-spinel-II can be considered as an
454 indicator of replacement during a dissolution-precipitation process following Putnis (2002). The
455 misorientation of only few degrees measured at the contact between Cr-spinel-II and ferritchromite is
456 thus interpreted as evidence for replacement of Cr-spinel-II by an assemblage composed of magnetite
457 and ferritchromite.

458 The microtextural and compositional information point thus towards spinel alteration sequence
459 proceeding in two stages. The magmatic spinel, (Cr,Al)-spinel-I, is first replaced during alteration
460 “Stage I” by a porous chromite, Cr-spinel-II, containing chlorite inclusions, which then reacted during
461 alteration “Stage II” to form magnetite and ferritchromite. This alteration sequence occurred in both the
462 host serpentinite and the magnetite ore. However, the spatial relationship (patches or reaction rims) and
463 the fraction of ferritchromite (high or restricted to a thin layer) differ between the two lithologies.
464 Thermodynamic modelling is used in the following to constrain the temperature and oxygen fugacity
465 having prevailed during the two aforementioned stages of alteration.

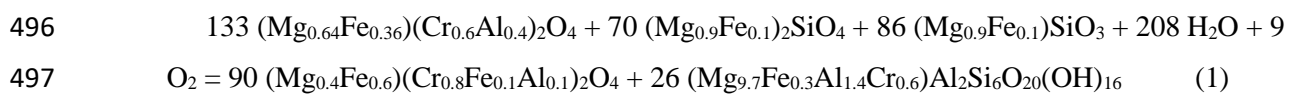
466

467 **7.2 Conditions prevailing during the alteration stages**

468 Thermodynamic modelling has been used in the past to predict the evolution of spinel
469 composition as a function of temperature. Gervilla et al. (2012) were able to predict the evolution of the
470 spinel X_{Cr} during alteration from the spinel solid solution model proposed by Klemme et al. (2009).
471 Colas et al. (2019) calculated the evolution of the spinel X_{Mg} with another solid-solution model based
472 on the ideal solid solution between Mg and Fe^{2+} on the tetrahedral site as proposed by Engi (1983).
473 These solid solutions either ignore ferric end-members (magnetite, $FeFe^{3+}_2O_4$, and magnesioferrite,
474 $MgFe^{3+}_2O_4$) or they consider ideal mixing between end-members. This has only minor consequences on
475 calculated high-temperature spinel compositions since spinel is Fe^{3+} -poor at high temperature. However,
476 the consideration of ideal mixing precludes for instance the prediction of the immiscibility gap between
477 magnetite and ferritchromite which is encountered towards low temperatures. We circumvented this
478 problem by introducing the mixing parameters of Sack and Ghiorso (1991) in a reciprocal solid-solution
479 model in *Perple_X* (Supplementary Materials 1). Thermodynamic modelling with this latter solid-
480 solution model in the Cr-CFMASH system with the composition of the Sabzevar serpentinite provides
481 insights on the temperature – $\Delta\log_{10}fO_2$ conditions prevailing during spinel alteration.

482 According to our thermochemical modelling, the composition of chromite is very sensitive to
483 temperature and $\Delta\log_{10}fO_2$, as suggested by Evans and Frost (1976). Simulation of spinel composition
484 during a cooling path from 800 down to 300 °C (500 MPa) associated with an increase from 0 to 2
485 followed by a decrease from 2 to -4 in $\Delta\log_{10}fO_2$, shows that the chromite composition drastically

486 changes at ~ 700 and ~ 450 °C (Fig. 12). At temperature above ~ 700 °C, a magmatic spinel-like
 487 composition is obtained with an X_{Cr} of 0.4 slightly higher than in the natural samples and an X_{Mg} close
 488 to 1 (Fig. 12). Below ~ 700 °C, X_{Cr} rapidly increases due to the formation of chlorite which incorporates
 489 aluminum. The silica necessary to form chlorite is provided by olivine and orthopyroxene. This
 490 predicted evolution of the spinel composition is in good agreement with the evolution occurring in the
 491 course of alteration “Stage I” as observed in the Sabzevar samples where porous Cr-spinel-II containing
 492 chlorite inclusions has formed at the expense of (Cr,Al)-spinel-I. Thermodynamic modelling constrains
 493 the alteration “Stage I” to temperatures and $\Delta\log_{10}fO_2$ comprised between 575 and 725 °C and 0 and 3,
 494 respectively. Based on thermodynamic modelling and the composition measured in the Sabzevar
 495 samples, the following reaction is proposed for “Stage I”:

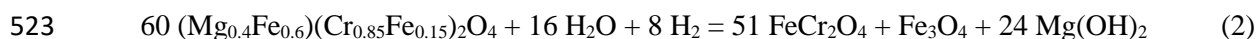


498 $Mg_{magmatic\ spinel} + olivine + orthopyroxene + water + oxygen = Cr\text{-}spinel\ II + chlorite$

499 The source of oxygen in the system is difficult to infer from the data and could be primary
 500 mineral reduction (pyroxene) or water dissociation. The reaction of one mole of magmatic spinel
 501 requires at least 1.2 times more moles of olivine and orthopyroxene to reach completion. Merlini et al.
 502 (2009) used image analysis on mineral assemblages having recorded a reaction similar to Reaction (1).
 503 They found a correlation between the volume of silicates initially present and the extent of reaction.
 504 This observation indicates that reaction progress depends on silica availability rather than on kinetics.
 505 In the Sabzevar ophiolite, the olivine + orthopyroxene over magmatic spinel amount ratio is much higher
 506 in the serpentinite than in the magnetite ore. However, magmatic spinel is only preserved in the
 507 serpentinite, suggesting that silica availability does not control reaction progress alone. The silica source
 508 to form chlorite is derived from olivine and orthopyroxene in Reaction (1) rather than antigorite as
 509 proposed by Merlini et al. (2009). This has fundamental implications for the inference of possible
 510 alteration scenarios. In the thermodynamic simulation provided here, the chlorite stability field can be
 511 entered either through cooling and olivine/orthopyroxene breakdown (retrograde metamorphism) or
 512 through heating and antigorite breakdown (prograde metamorphism). We found that the samples of the
 513 Sabzevar ophiolite experienced two alteration stages with first the production of Cr-spinel II at the
 514 expense of (Cr,Al)-spinel I and then the development of a reaction rim composed of Fe-chromite
 515 ($FeCr_2O_4$) and magnetite (Fe_3O_4) around Cr-spinel II. Thermodynamic modelling predicts that alteration
 516 Stage I occurs at approximately 650 °C and alteration Stage II below 430 °C (Figs 11 and 12). The
 517 reaction sequence observed here thus proceeded upon cooling.

518 The thermodynamic simulation also predicts the formation of brucite during alteration “Stage
 519 II”, in agreement with the observations in the serpentinite from the Sabzevar ophiolite Fig. S7. Mg
 520 depletion from spinel is compensated through ferric iron reduction to form magnetite according to the

521 following reaction based on the compositions measured in the Sabzevar samples (in which Al is not
522 considered for simplicity):



524 Cr-Spinel II + water + dihydrogen = ferritchromite + magnetite + brucite end member

525 Reaction 2 is $f\text{O}_2$ dependent and is favored by reducing conditions, i.e., higher H_2 partial
526 pressures. This is consistent with the thermodynamic modelling which indicates that the serpentine +
527 brucite + ferritchromite + magnetite assemblage is only stable at $\Delta\log_{10}f\text{O}_2$ below 2. Serpentinization of
528 olivine during mantle-rock alteration is known to produce H_2 in the same temperature range as reaction
529 (2) (McCollom and Bach, 2009). It leads to extremely reducing conditions favoring the precipitation of
530 Fe-Ni alloys (e.g., awaruite; Frost, 1985; Klein and Bach, 2009). We observed awaruite as tiny grains
531 ($<2 \mu\text{m}$) close to Cr-spinel-II crystals in the serpentinites of the Sabzevar ophiolite (Fig. S8), suggesting
532 that the reducing conditions imposed by serpentinization promoted Reaction (2) below $\sim 400^\circ\text{C}$.

533 Reaction (2) produces a volume of ferritchromite which is 57 times larger than the volume of
534 produced magnetite assuming isochemical conditions. This is not consistent with our observation of the
535 magnetite ore where ferritchromite rims are approximately two orders of magnitude thinner than the
536 magnetite rims. This implies that alteration “Stage II” is not isochemical in the magnetite ore and it
537 should involve either Cr depletion or Fe addition. Alteration “Stage II” thus occurred under open system
538 conditions with mass transfer at least over the size of the magnetite ore bodies ($> 0.5 \text{ m}$). We use in the
539 following the observed microtextures to provide additional constraints on the mobility of these two
540 elements.

541

542 **7.3 Chromite microtexture formation and element mobility**

543 The formation of hydrous phases (chlorite, serpentine and brucite) during spinel alteration
544 implies the presence of an aqueous fluid. Dissolution-precipitation occurring at the mineral interfaces is
545 an efficient process to promote metamorphic reactions and mineral replacement reaction (Putnis and
546 Austrheim, 2010). This type of process will be favored to interpret spinel alteration in the Sabzevar
547 ophiolite.

548 Our dataset indicates that Cr-spinel-II either forms a porous texture or homogeneous grains.
549 Based on the preservation of magmatic spinel cores rimmed by porous Cr-spinel-II, the development of
550 Cr-spinel-II porous textures seems to imply the inward migration of the magmatic spinel – fluid
551 boundary accompanied by the in-situ precipitation of the secondary products (mainly Cr-spinel-II and
552 chlorite) at constant Cr and Al content. Cr, which is present as Cr(III), and Al display both low
553 concentration and low diffusivity, they are thus expected to be mostly immobile. Note that this general

554 scheme does not apply if ligands that will complex Al and Cr are present (Huang et al., 2019). These
555 aqueous species have not been considered in our thermochemical modelling. We do not see an indication
556 for such complexation and suggest that the formation of porous textures is controlled by dissolution-
557 precipitation reactions and the limited mobility of Cr and Al compared to that of aqueous Si, Fe and Mg.

558 The assumption of low Cr and Al mobility used to explain porous replacement textures is
559 challenged by the fact that Cr-spinel-II can also be present as homogeneous area with a size up to 20
560 μm , with no obvious co-precipitation features.

561 Owing to the large temperature range estimated for alteration “Stage II”, these larger Cr-spinel-
562 II grains may have formed at the highest temperatures under which diffusive transport is more efficient.
563 Cr and Al transport over larger distances (sub-cm scale) may have been enhanced locally by advection
564 channels. Species transport may also depend on the initial microstructure of the (Al,Cr)-spinel-I which
565 seems to be highly variable in podiform chromitites (Leblanc, 1980).

566 Alteration “Stage II” in the serpentinite preserves the patchy texture with small Fe-chromite and
567 magnetite grains locally growing at the expense of Cr-spinel-II. In the magnetite ore, such a patchy
568 texture is not encountered since Fe-chromite and magnetite are not found as isolated grains but rather as
569 continuous rims surrounding the entire homogeneous or porous Cr-spinel II grains (Fig. 3, 5 and 6).
570 Such a difference in microtexture may be inherited from the alteration “Stage I” during which
571 homogeneous grains were more prone to form in the magnetite ore than in the serpentinite. The porous
572 texture may favor fluid access and chemical exchange in the serpentinite in comparison to the less
573 permeable homogeneous texture found in the magnetite ore. In the magnetite ore, the successive
574 occurrence of Cr-spinel-II, Fe-chromite and magnetite from the grain center to the rim recalls previous
575 observations in altered ultramafic rocks (Ulmer, 1974; Wylie et al., 1987; Michailidis, 1990; Prabhakar
576 and Bhattacharya, 2013; Barra et al., 2014; Colas et al., 2019). Prabhakar and Bhattacharya (2013)
577 interpreted the formation of ferritchromite as a result of intercrystalline diffusion between Cr-spinel-II
578 and magnetite formed during serpentinization. The changes in composition observed here at the Cr-
579 spinel-II – ferritchromite and ferritchromite – magnetite interfaces are sharp, even at the nanoscale,
580 which is inconsistent with diffusion (Fig. 7 and 8). Ulmer (1974) observed a similar texture but with a
581 larger ferritchromite rind and thus also ruled out a diffusion process based on the same textural
582 argument. The interpretation of Prabhakar and Bhattacharya (2013) was based on the fact that the
583 magnetite outer rim does not mimic the Cr-spinel-II rim, as it would be expected for a replacement
584 reaction (Putnis, 2002). We observed the same digitized outer rim of magnetite here. However, based
585 on elemental X-ray maps (Fig. 5 and 6), collected on the magnetite rim, two distinct magnetite
586 generations of different composition can be distinguished. The first type (magnetite-I) in contact with
587 ferritchromite is Si-poor and Ti- and V-rich. Magnetite-I is surrounded by a second magnetite generation
588 (magnetite-II). The interface between magnetite-I and magnetite-II is sharp and angular and mimics the

589 shape of Cr-spinel-II. Pseudomorphic replacement is confirmed by the small misorientation between Cr-
590 spinel-II and ferritchromite across their common interface. These observations indicate that
591 ferritchromite and magnetite-I are formed through a replacement process (Wylie et al., 1987) during
592 alteration Stage II. The spatial distribution of ferritchromite and magnetite suggests the presence of
593 chemical potential gradients during precipitation. As for alteration “Stage I”, the calculated Cr solubility
594 is low and the dissolved Cr species are trivalent during alteration “Stage I”. Fe is mainly divalent and
595 several orders of magnitude more soluble than Cr. This promotes slow and fast Cr and Fe transports,
596 respectively. As a result, a strong chemical potential gradient in Cr₂O₃ is expected to develop during the
597 alteration of the Cr-spinel-II whereas the chemical potential gradient in FeO, if any, is expected to be
598 smooth. This generates a supersaturation in ferritchromite only in the vicinity of Cr-spinel-II. The small
599 thickness of ~ 1 μm measured here for the ferritchromite indicates that Cr was almost immobile during
600 the alteration and that the dissolution of Cr-spinel-II was extremely slow, in agreement with the low
601 temperature inferred for alteration “Stage II”. In such conditions, the initial surface of the Cr-spinel-II
602 grain is expected to be close from the actual position of the ferritchromite – magnetite contact. The
603 presence of ferritchromite with a crystal structure and unit-cell parameters similar to magnetite can be
604 used as a template for magnetite growth. Such an epitaxial growth of magnetite on ferritchromite is
605 energetically favored since it circumvents the need for nucleation (Fig. 8). The observation of a second
606 magnetite type (magnetite-II), with no orientation relationship with ferritchromite and magnetite-I
607 suggests that magnetite could also precipitate in the serpentine/chlorite matrix during the alteration
608 “Stage II” (Fig. 8 and 9). The differences in composition measured at the micrometer scale between
609 magnetite-I and magnetite-II is no longer observed at the nanometer scale but Ti-rich and silicate
610 inclusions have been found in magnetite-I and -II, respectively (Fig. 10; Deditius et al., 2018).
611 Magnetite-I does not contain silicate inclusions but displays a silica content of ~ 1.23 wt.% (Fig. 5 and
612 10), indicating that Si is also incorporated in the magnetite structure. As a result, the micrometer-scale
613 difference in composition between magnetite-I and magnetite-II does not necessary reflect a difference
614 in fluid composition or temperature during precipitation. It rather indicates different growth mechanisms
615 (pseudomorphism or not) and different locus of precipitation (Cr-spinel II surface or silicate-rich
616 matrix). Silican magnetite has been reported in a wide range of rocks including ultramafic rocks, igneous
617 rocks and banded iron formations (Huberty et al., 2012 and references therein). Ciobanu et al. (2019)
618 have recently reported pseudomorphic rutile inclusions and Mg-bearing silicate inclusions in magnetite,
619 similar to the one reported here.

620 **7.4 Iron mobility and magnetite ore formation**

621 Several genetic processes have been invoked for the genesis of serpentinite-hosted magnetite
622 deposits: (i) precipitation from a high-temperature (~300–400 °C) fluid in a hydrothermal system (e.g.
623 Toffolo et al., 2017.; Khedr and Arai, 2018) ; (ii) low-*T* (100–300 °C) serpentinitization at high water-
624 rock ratio (e.g. Gahlan et al., 2006; Eslami et al., 2018a); and (iii) metamorphic transformation of pre-

625 existing chromitite with magmatic origin into magnetite (e.g. Paraskevopoulos and Economou, 1980;
626 Rossetti et al., 2009).

627 The dataset presented here provides additional important constraints on the formation of
628 magnetite ore bodies. Magnetite-I and magnetite-II are formed here during alteration “Stage II” at
629 temperature below 430 °C and in reducing conditions (oxygen fugacity below the FMQ buffer). These
630 conditions are compatible with serpentinization during which the iron initially contained in olivine and
631 pyroxene is incorporated as Fe²⁺ in serpentine and brucite or oxidized and incorporated as Fe³⁺ in
632 magnetite and serpentine (McCollom et al., 2009). The distribution of iron between the reaction products
633 is mainly controlled by temperature, with magnetite being the main iron carrier at temperature above
634 200 °C (Klein et al., 2009; Malvoisin et al., 2012; Klein et al., 2014). The first magnetite grains formed
635 in hydrothermal processes such as early serpentinization, are likely nano-sized and thus highly reactive
636 (Brunet, 2019). Bach et al. (2006) and Beard et al. (2009) found in serpentinites from the Mid-Atlantic
637 Ridge that iron first precipitates in brucite in the core of the meshes formed during olivine
638 serpentinization. Also, submicrometer magnetite grains have been observed in similar mesh cores
639 observed in natural samples (Rouméjon et al., 2018; Liu et al., 2019; Malvoisin et al., 2020). Iron is then
640 re-mobilized during the dissolution of brucite or tiny magnetite grains and transported out of the center
641 and towards the border of the meshes where magnetite precipitates. Maffione et al. (2014) used magnetic
642 and petrographic data to show that nanograins of magnetite are formed in the incipient stages of
643 serpentinization. The grain size then increases to reach several micrometers at higher serpentinization
644 degrees. Malvoisin and Brunet (2014) reported the formation of both submicrometer and tens of
645 micrometer-wide magnetite grains during experiments of dunite serpentinization. Iron is thus
646 transported at least at the hundreds of micrometer scale during serpentinization.

647 Alteration “Stage II” in the magnetite ore provides constraints on the extent of iron mobility
648 during serpentinization. This stage should indeed produce a factor of 57 more ferritchromite than
649 magnetite in volume if the reaction was occurring in a closed system according to Reaction (2). This
650 proportion is at odds with the observed 50 to 100 µm-wide rim of magnetite-I + magnetite-II and 1 µm-
651 thick rind of ferritchromite at the Cr-spinel II surface. Such a phase proportion requires a pronounced
652 mass transfer between the magnetite ore body and its surrounding, most likely the host serpentinite. We
653 showed above that Cr is immobile and Fe is the main element to be transferred to the magnetite ore. Fe
654 probably originated from direct transport of the Fe²⁺ produced during olivine dissolution or from the
655 dissolution of nanosized magnetite grains initially formed in the host serpentinite during early
656 serpentinization (Brunet, 2019). Thermodynamic modelling reveals that the iron content measured in
657 the Sabzevar serpentinite is too low to reproduce the Mg/(Mg+Fe) ratio measured in olivine relicts,
658 suggesting that iron is lost in the peridotite during alteration. Iron transfer requires an iron chemical
659 potential gradient between the host serpentinite and the magnetite ore. Such a gradient can be generated
660 if the energetic barrier to overcome for magnetite precipitation is lower in the magnetite ore than in the

661 serpentine host. Three processes can contribute to reduce the energetic barrier at the spinel surface. As
 662 discussed above, the similarities in crystal structure first allow for an epitaxial growth of magnetite over
 663 Cr-spinel -II without a need for nucleation (Fig. 9). The growth of the tens of micrometer-wide spinel
 664 grains in the magnetite ore is also favored by their smaller interfacial energy compared to the nanograins
 665 of magnetite formed during serpentinization (Ostwald ripening). Magnetite formation during
 666 serpentinization also requires electron transfer from Fe^{2+} to water, leading to water splitting and H_2
 667 formation. Spinel-structure minerals have been proposed to catalyze this process (Mayhew et al., 2013)
 668 due to the high mobility of electrons in their structure (Hamilton, 1958; Skomurski et al., 2010) and to
 669 the possibility to sorb water at the spinel surface (Kendelewicz et al., 2000; Parkinson et al., 2011).

670 We aim in the following at calculating the amount of olivine necessary to form the magnetite
 671 ore bodies observed in the Sabzevar ophiolite. On the two-dimensional outcrop, magnetite ore bodies
 672 occur as boudins with a thickness of $L_{\text{ore}} \sim 0.5$ m hosted in a serpentine. We assume in the following
 673 that the thickness of the magnetite ore is also ~ 0.5 m in the third direction, that the serpentine was
 674 initially a dunite composed of olivine (Fo_{90}) and that all the iron initially contained in olivine has been
 675 transported up to the magnetite ore according to a simplified reaction: $2(\text{Mg}_{0.9}, \text{Fe}_{0.1})_2\text{SiO}_4 + 2.2 \text{H}_2\text{O} +$
 676 $0.8 \text{H}^+ \Rightarrow \text{Mg}_3\text{Si}_2\text{O}_5(\text{OH})_4 + 0.6 \text{Mg}(\text{OH})_2 + 0.4 \text{Fe}^{2+}_{\text{aq}}$. This latter reaction implies that, in the host-
 677 serpentine, no Fe is incorporated into lizardite and brucite and that no magnetite is formed. Under these
 678 assumptions, the minimum thickness of dunite necessary to form the ore bodies can be expressed as:

679

$$680 \quad L_{\text{dun}} = \frac{3vL_{\text{ore}}V_{\text{mol}}}{2X\text{Fe}V_{\text{mmag}}} \quad (3)$$

681 where v is the volume fraction of magnetite in the ore bodies (90 vol. %) and V_{mol} and V_{mmag} are the
 682 molar volume of olivine and magnetite, respectively ($V_{\text{mol}} = 44.73 \text{ cm}^3/\text{mol}$ and $V_{\text{mmag}} =$
 683 $44.56 \text{ cm}^3/\text{mol}$). Equation (3) leads to an estimated dunite thickness of 6.8 m. This estimate is a
 684 minimum, as it is assumed that all iron is lost from the dunite. The bulk iron content measured in the
 685 Sabzevar serpentine is around 20 % lower than the amount necessary to reproduce the measured olivine
 686 composition with our thermodynamic modelling. Considering such a Fe loss would lead to a dunite
 687 thickness of ~ 30 m. Iron transport at a scale > 10 m requires, in addition to the chemical potential
 688 gradient in iron, an efficient transport mechanism. We observe shear zones in the magnetite ore but not
 689 in the host serpentine, suggesting that advection cannot explain alone iron transfer. The diffusivity of
 690 Fe^{2+} in a free fluid at 300°C and 100 MPa is $\underline{D} \sim 10^{-8} \text{ m}^2/\text{s}$ (Oelkers and Helgeson, 1988). It can be used
 691 to calculate a characteristic time for diffusion (τ) over a distance $x = 10$ m of $\tau = \frac{x^2}{D} = 300$ yr. This
 692 duration is a lower bound for diffusive iron transport as diffusion is slower at grain boundary than in a
 693 free fluid. Nevertheless, it indicates that diffusion is a possible mechanism for the observed segregation
 694 of iron.

695 The mechanism of magnetite ore formation proposed here involves limited chromium transport
696 and chromite dissolution. As a result, the current amount of chromite in the magnetite ore is probably
697 similar to the amount of chromite before alteration. Chromite now represents approximately 5 vol.% of
698 the magnetite ore. This corresponds to a thickness of 2.5 cm for a pure chromitite layer. The chromitite
699 was probably not exclusively composed of chromite but rather occurred as a disseminated chromitite.

700 **8. Scenario of spinel alteration – magnetite formation**

701 Based on textural observation at micro- and nano-scales, as well as thermodynamic modelling,
702 the Sabzevar magnetite ores and their host serpentinites are shown to have recorded two events of spinel
703 alteration (Fig. 14). The presence of a non-metamorphic volcanogenic massive-sulfide (VMS)
704 mineralization, and sea-floor alteration recorded in basaltic sequences of the Sabzevar ophiolite
705 precludes the possibility of high-grade obduction-related metamorphism in the area. A first stage of
706 alteration is ascribed to the formation of porous Cr-spinel II with chlorite inclusions at the expense of
707 magmatic spinel. Temperatures and $\Delta\log_{10}fO_2$ of alteration “Stage I” obtained using our new
708 thermodynamic modelling range between 725 and 575 °C and between 0 and 3, respectively. These
709 conditions are compatible with high-temperature hydrothermal circulation of seawater at mid-ocean
710 ridges at depth, as suggested by Tao et al. (2020) and Hasenclever et al. (2014). A second stage of
711 alteration is marked by the development of a reaction rim consisting of ferritchromite ($FeCr_2O_4$),
712 magnetite (Fe_3O_4) and brucite at the expense of porous Cr-spinel-II at temperatures below 400 °C and
713 $\Delta\log_{10}fO_2 < -2$. This reaction is fO_2 dependent and favored by the presence of H_2 . The second alteration
714 stage is interpreted as the serpentinization of the Sabzevar oceanic peridotite during progressive
715 exhumation of mantle peridotite and associated chromitite ore deposits. Therefore, unless additional
716 geochemical data are collected to constrain with origin of the alteration aqueous fluid, we favor a simple
717 geodynamic scenario of seawater/rock interaction during progressive exhumation of a mantle segment
718 including chromitite bodies to account for the spinel alteration and the formation of the Sabzevar
719 magnetite orebodies. Although there are no structural data on the study area, re-activation of oceanic
720 faults can be expected for the remarkable hydrothermal alteration of chromitite bodies and associated
721 peridotites in the study area. Low modal abundances of Cr-spinel relicts in the Sabzevar magnetite ore
722 revealed that they may derive from disseminated chromitite protoliths during these two stages of spinel
723 alteration.

724 **9. Concluding remarks**

725 Sabzevar magnetite ores and their host serpentinites recorded two events of spinel alteration. The first
726 alteration stage occurred at temperatures between 725 and 575 °C and led to chlorite and Al-free Cr-
727 spinel formation. The second alteration stage occurred during serpentinization at temperature < 400 °C
728 and is associated with magnetite precipitation. The two alteration stages probably successively occurred
729 during mantle-rock exhumation from depth at a mid-ocean ridge. During spinel alteration and magnetite

730 ore formation, chromium mobility is extremely low and chromite dissolution is limited. Orientation
731 mapping at the nanoscale reveals epitaxial growth of ferritchromite and magnetite on Cr-spinel II. This
732 is interpreted as evidence for a coupled Cr-spinel II dissolution-ferritchromite + magnetite precipitation
733 process. Olivine breakdown and/or dissolution of nanoscale magnetite grains initially formed in the host
734 serpentinite provided the iron necessary for magnetite ore formation. Mass balance calculations indicate
735 iron transport over distances beyond 10 meters during serpentinization.

736 **Acknowledgment**

737

738 This research was partially supported by Iran National Science Foundation (INFS), to whom we are
739 indebted. The authors would like to express their sincere appreciation to the editor Prof. Dante Canil
740 and one anonymous referee whose careful comments and useful criticisms greatly improved the
741 manuscript.

742 **References**

- 743 Barra F, Gervilla F, Hernández E, Reich M, Padrón-Navarta JA, González-Jiménez JM (2014)
744 Alteration patterns of chromian spinels from La Cabaña peridotite, south-central Chile. *Mineral Petrol*
745 108(6): 819-836.
- 746 Beard JS, Frost BR, Fryer P, McCaig A, Searle R, Ildefonse B, Zinin P, Sharma SK (2009) Onset and
747 progression of serpentinization and magnetite formation in olivine-rich troctolite from IODP Hole
748 U1309D. *J Petrol* 50(3): 387-403.
- 749 Brunet F (2019) Hydrothermal production of H₂ and magnetite from steel slags: a geo-inspired approach
750 based on olivine serpentinization. *Front Earth Sci* 7: 17.
- 751 Colás V, González-Jiménez JM, Camprubí A, Proenza JA, Griffin WL, Fanlo I, O'Reilly SY, Gervilla
752 F, González-Partida E (2019) A reappraisal of the metamorphic history of the Tehuiztzingo chromitite,
753 Puebla state, Mexico. *Int Geol Rev* 61(14): 1706-1727.
- 754 Ciobanu CL, Verdugo-Ihl MR, Slattery A, Cook NJ, Ehrig K, Courtney-Davies L, Wade BP (2019)
755 Silician magnetite: Si-Fe-Nanoprecipitates and other mineral inclusions in magnetite from the Olympic
756 dam deposit, South Australia. *Minerals* 9(5): 311.
- 757 Deditius AP, Reich M, Simon AC, Suvorova, A, Knipping J, Roberts MP, Rubanov S, Dodd A, Saunders
758 M (2018) Nanogeochemistry of hydrothermal magnetite. *Contrib Mineral Petrol* 173: 46.
759 <https://doi.org/10.1007/s00410-018-1474-1>.
- 760 Dick HJ, Bullen T (1984) Chromian spinel as a petrogenetic indicator in abyssal and alpine-type
761 peridotites and spatially associated lavas. *Contrib Miner Petrol* 86(1): 54-76.
- 762 Engi M (1983) Equilibria involving Al-Cr spine: Mg-Fe exchange with olivine. Experiments,
763 thermodynamic analysis, and consequences for geothermometry. *Am J Sci* 284-A, 29-71.
- 764 Eslami A, Arai S, Miura M, Mackizadeh MA (2018a) Metallogeny of the mantle-hosted magnetite ores
765 of the Nain ophiolite, Central Iran: implications for high mobility and re-concentration of Fe promoted
766 by multi-episodic serpentinization. *Ore Geol Re* 95: 80-694.
- 767

- 768 Eslami A, Grieco G, Davoudi M (2018b) Preliminary geochemical studies of podiform chromitites in
769 the Cheshmeh-Khan Mining District, central sector of Sabzevar ophiolite belt, NE Iran. 8th
770 Geochemistry Symposium (2018), Antalya, Turkey.
771
- 772 Frost BR (1985) On the stability of sulfides, oxides, and native metals in serpentinite. *J Petrol* 26(1): 31-
773 63.
- 774 Gahlan HA, Arai S (2007) Genesis of peculiarly zoned Co, Zn and Mn-rich chromian spinel in
775 serpentinite of Bou-Azzer ophiolite, Anti-Atlas, Morocco. *J Mineral Petrol Sci* 102: 69-85.
- 776 Gahlan HA, Arai S, Ahmed AH, Ishida Y, Abdel-Aziz YM, Rahimi A (2006) Origin of magnetite veins
777 in serpentinite from the Late Proterozoic Bou-Azzer ophiolite, Anti-Atlas, Morocco: An implication for
778 mobility of iron during serpentinitization. *J African Earth Sci* 46: 318–330.
- 779 Galvez ME, Manning CE, Connolly JAD, Rumble D (2015) The solubility of rocks in metamorphic
780 fluids: A model for rock-dominated conditions to upper mantle pressure and temperature. *Earth Planet*
781 *Sci Lett* 1: 1–13, doi:10.1016/j.epsl.2015.06.019.
- 782 Galvez ME, Connolly JA, Manning CE (2016) Implications for metal and volatile cycles from the pH
783 of subduction zone fluids. *Nature* 539(7629): 420-424.
- 784 Gervilla F, Padrón-Navarta JA, Kerestedjian T, Sergeeva I, González-Jiménez JM, Fanlo I (2012)
785 Formation of ferrian chromite in podiform chromitites from the Golyamo Kamenyane serpentinite,
786 Eastern Rhodopes, SE Bulgaria: a two-stage process. *Contrib Miner Petrol* 164(4): 643-657.
- 787 Hamilton W (1958) Neutron diffraction investigation of the 119K Transition in Magnetite. *Phys Rev*
788 110: 1050–1057.
- 789 Hasenclever J, Theissen-Krah S, Rüpke LH, Morgan JP, Iyer K, Petersen S, Devey CW (2014) Hybrid
790 shallow on-axis and deep off-axis hydrothermal circulation at fast-spreading ridges. *Nature*
791 508(7497):508-12. doi: 10.1038/nature13174. PMID: 24759413.
- 792 Holland TJB, Powell R (2011) An improved and extended internally consistent thermodynamic dataset
793 for phases of petrological interest, involving a new equation of state for solids. *J Metamorph Geol* 29:
794 333–383, doi:10.1111/j.1525-1314.2010.00923.x.
- 795 Holland TJB, Powell R (1998) An internally consistent thermodynamic data set for phases of
796 petrological interest. *J Metamorph Geol* 16: 309–343, doi:10.1111/j.1525-1314.1998.00140.x.
- 797 Holland T, Powell R (1996) Thermodynamics of order-disorder in minerals; II, Symmetric formalism
798 applied to solid solutions. *Ame Miner* 81: 1425–1437.
- 799 Huang J, Hao J, Huang F, Sverjensky DA (2019) Mobility of chromium in high temperature crustal and
800 upper mantle fluids: *Geochem Perspect Lett* 12:1–6, doi:10.7185/geochemlet.1926.
- 801 Huberty JM, Konishi H, Heck PR, Fournelle JH, Valley JW, Xu H (2012) Silician magnetite from the
802 Dales Gorge member of the Brockman iron formation, Hamersley Group, Western Australia. *Am*
803 *Miner* 97(1): 26-37.
- 804 Kendelewicz T, Liu P, Doyle CS, Brown Jr GE, Nelson EJ, Chambers SA (2000) Reaction of water with
805 the (100) and (111) surfaces of Fe₃O₄. *Surf Sci* 453: 32–46.
806
- 807 Khedr MZ, Arai S (2018) Composite origin of magnetite deposits hosted in Oman peridotites: Evidence
808 for iron mobility during serpentinitization. *Ore Geol Rev* 101: 180–198. <https://doi-org.gaelnomade-1.grenet.fr/10.1016/j.oregeorev.2018.07.003>.

- 810 Kimball KL (1990) Effects of hydrothermal alteration on the compositions of chromian spinels. *Contrib*
811 *Miner Petrol* 105(3): 337-346.
- 812 Klemme S, Ivanic TJ, Connolly JAD, Harte B (2009) Thermodynamic modelling of Cr-bearing garnets
813 with implications for diamond inclusions and peridotite xenoliths: *Lithos* 112: 986–991,
814 doi:10.1016/j.lithos.2009.05.007.
- 815 Klein F, Bach W (2009) Fe–Ni–Co–O–S phase relations in peridotite–seawater interactions. *J Petrol*
816 50(1): 37-59.
- 817 Klein F, Bach W, Jöns N, McCollom T, Moskowitz B, Berquó T (2009) Iron partitioning and hydrogen
818 generation during serpentinization of abyssal peridotites from 15 N on the Mid-Atlantic Ridge. *Geochim*
819 *Cosmochim Acta* 73(22): 6868-6893.
- 820 Klein F, Bach W, Humphris SE, Kahl WA, Jöns N, Moskowitz B, Berquó TS (2014) Magnetite in
821 seafloor serpentinite—Some like it hot. *Geology* 42(2): 135-138.
- 822
- 823 Klemme S, Ivanic TJ, Connolly JAD, Harte B (2009) Thermodynamic modelling of Cr-bearing garnets
824 with implications for diamond inclusions and peridotite xenoliths. *Lithos* 112:986–991.
- 825 Liu ZB, Li JC, Zhao T, Song Y, Yuan GL, Lin Y, Shao HS (2020) Serpentinisation and magnetite
826 formation in the Angwu ultramafic rocks from the central Bangong–Nujiang suture zone, Tibetan
827 Plateau. *Geol J* 55(2): 1283-1299.
- 828 Malvoisin B, Zhang C, Müntener O, Baumgartner LP, Kelemen PB, Oman Drilling Project Science
829 Party (2020) Measurement of Volume Change and Mass Transfer During Serpentinization: Insights
830 From the Oman Drilling Project. *J Geophys Res Solid Earth* 125(5), e2019JB018877.
- 831 Malvoisin B, Carlut J, Brunet F (2012) Serpentinization of oceanic peridotites: 1. A high-sensitivity
832 method to monitor magnetite production in hydrothermal experiments. *J Geophys Res Solid Earth*
833 117(B1).
- 834 Mellini M, Rumori C, Viti C (2005) Hydrothermally reset magmatic spinels in retrograde serpentinites:
835 formation of “ferritchromit” rims and chlorite aureoles. *Contrib Miner Petrol* 149: 266–275.
- 836 Merlini A, Grieco G, Diella V (2009) Ferritchromite and chromian-chlorite formation in mélange-hosted
837 Kalkan chromitite (Southern Urals, Russia). *Am Miner* 94: 1459-1467.
- 838 Michailidis KM (1990) Zoned chromites with high Mn-contents in the Fe-Ni-Cr-laterite ore deposits
839 from the Edessa area in Northern Greece. *Miner Deposita* 25(3): 190-197.
- 840 Moody JB (1976) An experimental study on the serpentinization of iron-bearing olivines. *Can*
841 *Mineral* 14(4): 462-478.
- 842 Mousivand F, Rastad E, Peter JM, Maghfouri S (2018) Metallogeny of volcanogenic massive sulfide
843 deposits of Iran. *Ore Geol Rev* 95: 974-1007.
- 844
- 845 Merlini A, Grieco G, Diella V (2009) Ferritchromite and chromian-chlorite formation in mélange-hosted
846 Kalkan chromitite (Southern Urals, Russia). *Am Miner* 94(10): 1459-1467.
- 847 McCollom TM, Bach W (2009). Thermodynamic constraints on hydrogen generation during
848 serpentinization of ultramafic rocks. *Geochim Cosmochim Acta* 73(3): 856-875.
- 849 Noghreyan M (1982) Evolution géochimique, mineralogique et structurale d’un edificeophiolitique
850 singulier: le massif de Sabzevar (partie centrale), NE de l’Iran. *TheseDoc. d’Etat, Université de Nancy,*
851 *France*, p. 239.

- 852 Omrani H (2018) Island-arc and active continental margin adakites from the Sabzevar Zone, Iran.
853 *Petrology* 26: 96–113. <https://doi.org/10.1134/S0869591118010058>
- 854 Padrón-Navarta JA, Sánchez-Vizcaíno VL, Hermann J, Connolly JAD, Garrido CJ, Gómez-Pugnaire
855 MT, Marchesi C (2013) Tschermak's substitution in antigorite and consequences for phase relations and
856 water liberation in high-grade serpentinites. *Lithos* 178: 186–196, doi:10.1016/j.lithos.2013.02.001.
- 857 Oelkers EH, Helgeson HC (1988) Calculation of the thermodynamic and transport properties of aqueous
858 species at high pressures and temperatures: Aqueous tracer diffusion coefficients of ions to 1000 C and
859 5 kb. *Geochim Cosmochim Acta* 52(1): 63-85.
860
- 861 O'Neil HSC, Wall VJ (1987) The Olivine—Orthopyroxene—Spinel oxygen geobarometer, the nickel
862 precipitation curve, and the oxygen fugacity of the Earth's Upper Mantle. *J Petrol* 28(6): 1169-1191.
- 863 Oufi O, Cannat M, Horen H (2002) Magnetic properties of variably serpentinized abyssal peridotites. *J*
864 *Geophys Res Solid Earth* 107(B5), EPM-3.
- 865 Paraskevopoulos GM, Economou MI (1980) Genesis of magnetite ore occurrences by metasomatism of
866 chromite ores in Greece. *Neues Jb Miner Abh* 140: 29–53.
- 867 Parkinson GS, Novotny Z, Jacobson P, Schmid M, Diebold U (2011) Room temperature water splitting
868 at the surface of magnetite RID A-3681-2010. *J Am Chem Soc* 133: 12650–12655.
- 869 Prabhakar N, Bhattacharya A (2013) Origin of zoned spinel by coupled dissolution–precipitation and
870 inter-crystalline diffusion: evidence from serpentinized wehrlite, Bangriposi, Eastern India. *Contrib*
871 *Miner Petrol* 166(4): 1047-1066.
- 872 Putnis A, Austrheim, H (2010) Fluid-induced processes: metasomatism and metamorphism. *Geofluids*
873 10(1-2): 254-269.
- 874 Rauch EF, Véron MJMC (2014) Automated crystal orientation and phase mapping in TEM. *Mater*
875 *Charact* 98: 1-9.
- 876 Rouméjon S, Früh-Green GL, Orcutt BN, IODP Expedition 357 Science Party (2018) Alteration
877 heterogeneities in peridotites exhumed on the southern wall of the atlantis massif (IODP expedition
878 357). *J Petrol* 59(7): 1329-1358.
- 879 Rahmani F, Mackizadeh MA, Noghreyan M, Marchesi C, Garrido CJ (2020) Petrology and
880 geochemistry of mafic and ultramafic cumulate rocks from the eastern part of the Sabzevar ophiolite
881 (NE Iran): Implications for their petrogenesis and tectonic setting. *Geosci Front* 11(6): 347-2364
- 882 Rossetti P, Gatta GD, Diella V, Carbonin S, Della Giusta A, Ferrario A (2009) The magnetite ore
883 districts of the southern Aosta Valley (Western Alps, Italy): a mineralogical study of metasomatized
884 chromite ore. *Mineral Mag* 73: 737–751.
- 885 Shafaii Moghadam H, Corfu F, Chiaradia M, Stern RJ, Ghorbani G (2014) Sabzevar Ophiolite, NE Iran:
886 progress from embryonic oceanic lithosphere into magmatic arc constrained by new isotopic and
887 geochemical data. *Lithos* 210–211: 224–241.
- 888 Shojaat B, Hassanipak AA, Mobasher K, Ghazi AM (2003) Petrology, geochemistry and tectonics of the
889 Sabzevar ophiolite, North Central Iran. *J Asian Earth Sci* 21: 1053–1067.
- 890 Spear FS (1993) *Metamorphic Phase Equilibria And Pressure–Temperature–Time Paths* Mineralogical
891 Society of America, Washington, DC, 799 pp.
- 892 Sack RO, Ghiorso MS (1991) Chromian spinels as petrogenetic indicators: Thermodynamics and
893 petrological applications. *Am Miner* 76(5-6): 827–847.

894 Santos JS, Doriguetto AC, Fernandes NG (2005) Magnesium aluminium chromite. *Acta Crystallogr C*
895 61(3): i27-i28.

896 Schindler M, Lussier AJ, Principe E, Mykytczuk N (2018) Dissolution mechanisms of chromitite:
897 Understanding the release and fate of chromium in the environment. *Am Miner* 103(2): 271-283.

898 Skomurski FN, Kerisit S, Rosso KM (2010) Structure, charge distribution, and electron hopping
899 dynamics in magnetite (Fe₃O₄) (100) surfaces from first principles. *Geochim Cosmochim Acta* 74:
900 4234–4248.

901 Sverjensky DA, Harrison B, Azzolini D (2014) Water in the deep Earth: The dielectric constant and the
902 solubilities of quartz and corundum to 60 kb and 1200 °C. *Geochim Cosmochim Acta* 129: 125–145,
903 doi:10.1016/J.GCA.2013.12.019.

904 Tao C, Seyfried Jr WE, Lowell RP, Liu Y, Liang J, Guo Z, Ding K, Zhang H, Liu J, Qiu L, Egorov I,
905 Liao S, Zhao M, Zhou J, Deng X, Li H, Wang H, Cai W, Zhang G, Zhou H, Lin J, Li W (2020) Deep
906 high-temperature hydrothermal circulation in a detachment faulting system on the ultra-slow spreading
907 ridge. *Nat Commun* 11:1300. <https://doi.org/10.1038/s41467-020-15062-w>.

908 Toffolo L, Nimis P, Martin S, Tumiati S, Bach W (2017) The Cogne magnetite deposit (Western Alps,
909 Italy): a Late Jurassic seafloor ultramafic-hosted hydrothermal system?. *Ore Geol Rev* 83: 103-126.

910 Wylie AG, Candela PA, Burke TM (1987) Compositional zoning in unusual Zn-rich chromite from the
911 Sykesville District of Maryland and its bearing on the origin of "ferritchromit". *Am Miner* 72(3-4): 413-
912 422.

913

914

915

916

917

918

919

920

921

922

923

924

925

926

927

928

929

930

931

932

933

934

935

936 **Figure Captions:**

937

938 Fig. 1. (a) Distribution of Mesozoic ophiolites in Iran; (b) Simplified geological map of the Sabzevar–
939 Forumad ophiolites (modified after Shafaii Moghadam et al., 2014); (c) Simplified geological map of
940 the study area in the eastern sector of Sabzevar ophiolite.

941

942 Fig. 2. (a) Boundins of magnetite ore-bodies hosted by highly sheared serpentinite in the Sabzevar
943 ophiolite; (b) Sharp contact (red dashed line) between magnetite ore-body and sheared serpentinite; (c)
944 Close-up view of aggregation of octahedral magnetite crystals embedded in pale-green serpentine.

945

946 Fig. 3. Backscattered -electron images of the Sabzevar host serpentinite (a-d) and magnetite ore (e-i).
947 (a) partly altered chromite; (b) anhedral porous chromite; (c) close-up of porous chromite with irregular
948 patches of Fe-chromite and associated serpentine and chlorite inclusions; (d) Skeletal andradite
949 surrounding chromian spinel; (e) Relict of porous chromian spinel with thick magnetite rim; (f) Porous
950 chromite associated with mylonitized magnetite; (g) Homogenous chromite with thick magnetite rim;
951 (h) Euhedral magnetite crystals associated with andradite; (i) Individual inclusion of pentlandite in
952 magnetite crystals from magnetite ore. Chr: chromian spinel; Mag: magnetite; Srp: serpentine; Chl:
953 chlorite; Adr: andradite; Pn: pentlandite.

954 Fig. 4. Compositional plots of spinels on (a) ternary diagram Cr-Al-Fe³⁺; (b) a X_{Cr} versus X_{Mg} diagram;
955 (c) Fe³⁺/(Fe³⁺+Fe²⁺) versus X_{Mg}. Reference fields of podiform chromitites in eastern sector of the
956 Sabzevar ophiolite (Shafaii Moghadam et al., 2015; Eslami et al. 2018; unpublished data from the first
957 author) are shown for comparison.

958

959 Fig. 5. Multi-element (WDS-EDS) mapping of homogeneous chromian spinel relict in magnetite ore
960 (sample MG15)

961 Fig. 6. Multi-element (WDS-EDS) mapping of a porous chromian spinel relict in magnetite ore (sample
962 MG15)

963 Fig. 7. Bright Field Image (a) and EDS-STEM element maps (b to g) of the Cr-spinel / magnetite I
964 contact. The scale bar is 500 nm. Fchr: ferritchromite. Mag I: Magnetite I.

965 Fig. 8. Orientation maps and selected area electron diffraction (SAED) in the reaction zone around Cr-
966 spinel. a: orientation map in the same region as Figure 7, in which the transition from Cr-spinel to
967 magnetite I is observed. b: supersimposed SAEDs of Cr-spinel and ferritchromite. c: superimposed
968 SAEDs of ferritchromite and magnetite I. d: orientation map in the same region as Figure 10 at the
969 magnetite I/magnetite II contact. e: colour-coded inverse pole figure used for displaying orientation in
970 a and d. The boundaries between the different phases were determined with the EDS-STEM maps. CrSp:
971 Cr-spinel; Fchr: ferritchromite. Mag I: magnetite I.

972

973 Fig. 9. High-resolution TEM images. a: contact between Cr-spinel and ferritchromite. b: contact between
974 magnetite I and magnetite II. The red lines indicate the main orientation of the lattice planes. CrSp: Cr-
975 spinel; Fchr: ferritchromite; Mag I: magnetite I; Mag II: magnetite II.

976

977 Fig. 10. Bright Field Image (a) and EDS-STEM element maps (b to d) of the magnetite I / magnetite II
978 contact. The arrows indicate the location of silicate inclusions in magnetite II. The scale bar is 500 nm.
979 Mag I : magnetite I; Mag II: magnetite II.

980 Fig. 11. T vs. $\Delta\log_{10}f_{O_2}$ section for the Sabzevar serpentinite composition. The symbols indicate an
981 expected evolution of $\Delta\log_{10}f_{O_2}$ during cooling. They corresponds to an internally buffered oxygen
982 fugacity (fixed by the olivine-Mg-silicate-spinel assemblage at $T > 420^\circ\text{C}$ and the peridotite + pure
983 water assemblage at $T < 420^\circ\text{C}$; see text for details). Stars are used as symbols when the calculation
984 predicts the formation of a single phase. When two immiscible solid solutions are predicted to form, the
985 composition is displayed with circles and diamonds for the Cr-rich and Fe^{3+} -rich solid solutions,
986 respectively. The same symbols are used to display spinel composition in Fig. 12a. The red bold line
987 separates the fields containing one (CrSp) and two (CrSp + Mt) spinels. The green bold line surrounds
988 the chlorite stability field. Gt: garnet; Brc: brucite; Atg: antigorite; CrSp: Cr-bearing spinel; Hem:
989 hematite; Ol: olivine; Mt: magnetite; Amp: amphibole; Cpx: clinopyroxene; Opx: orthopyroxene; Tlc:
990 talc; Chl: chlorite.

991 Fig. 12. Evolution of spinel composition during cooling and oxygen fugacity decrease. The composition
992 is displayed along a typical peridotite cooling path. The temperature and $\Delta\log_{10}f_{O_2}$ conditions along this
993 path are provided in Fig. 11 with the same symbols. a; calculated composition in the Cr-Al- Fe^{3+}
994 ternary diagram. Stars are used as symbols when the calculation predicts the formation of a single phase. When
995 two immiscible solid solutions are predicted to form, the composition is displayed with circles and
996 diamonds for the Cr- rich and Fe^{3+} -rich solid solutions, respectively. b: calculated $\text{Mg}/(\text{Mg}+\text{Fe}^{2+})$ ratio
997 and brucite molar fraction along the investigated path. The $\text{Mg}/(\text{Mg}+\text{Fe}^{2+})$ ratios of the Cr- rich and
998 Fe^{3+} -rich spinel solid solutions are displayed with dashed and plain lines, respectively.

999 Fig. 13. Solubilities (mol/kg) as a function of temperature along the cooling path (see text and Fig. 11
1000 for details about the path). a: Fe solubility. b: Cr solubility.

1001 Fig. 14. Schematic evolution of spinel alteration in the Sabzevar serpentinite-hosted magnetite deposit
1002 and associated peridotites

1003
1004 A.E. acknowledges a financial support (Cotutelle Scholarship) from the Embassy of France in Tehran.
1005 Nathaniel Findling, Valérie Magnin and Valentina Batanova (ISTerre) are acknowledged for their help
1006 with Scanning Electron Microscopy and Electron Microprobe Analysis. G. Renou (CMTC, Grenoble) is
1007 thanked for help with transmission electron microscopy. This work has been supported by a grant
1008 from LabEx OSUG@2020 (Investissements d'avenir – ANR10 LABX56).

1009

1010 **Table Captions:**

1011 Table S1. Representative analyses of spinels from the Sabzevar host serpentinite

1012 Table S2. Representative analyses of spinels from the Sabzevar magnetite ore. Homogeneous Cr-spinel
1013 relict (grain B) from the sample MG15 were selected for TEM

1014 Table. S3. Representative analyses of sulfides and alloys in the Sabzevar magnetite ore and host
1015 serpentinite

1016 Table S4. Representative analyses of andradite from the Sabzevar magnetite ore and host serpentinite

1017 Table S5. Representative analyses of chlorite inclusions in chromites from the Sabzevar magnetite ore
1018 and host serpentinites.

1019

1020

1021

1022

1023

1024